nature protocols

REVIEW ARTICLE

https://doi.org/10.1038/s41596-020-0360-2

Tutorial: avoiding and correcting sample-induced spherical aberration artifacts in 3D fluorescence microscopy

Erin E. Diel[1], Jeff W. Lichtman[1,2,3] and Douglas S. Richardson[1,2]✉

Spherical aberration (SA) occurs when light rays entering at different points of a spherical lens are not focused to the same point of the optical axis. SA that occurs inside the lens elements of a fluorescence microscope is well understood and corrected for. However, SA is also induced when light passes through an interface of refractive index (RI)-mismatched substances (i.e., a discrepancy between the RI of the immersion medium and the RI of the sample). SA due to RI mismatches has many deleterious effects on imaging. Perhaps most important for 3D imaging is that the distance the image plane moves in a sample is not equivalent to the distance traveled by an objective (or stage) during *z*-stack acquisition. This non-uniform translation along the *z* axis gives rise to artifactually elongated images (if the objective is immersed in a medium with a higher RI than that of the sample) or compressed images (if the objective is immersed in a medium with a lower RI than that of the sample) and alters the optimal axial sampling rate. In this tutorial, we describe why this distortion occurs, how it impacts quantitative measurements and axial resolution, and what can be done to avoid SA and thereby prevent distorted images. In addition, this tutorial aims to better inform researchers of how to correct RI mismatch–induced axial distortions and provides a practical ImageJ/Fiji-based tool to reduce the prevalence of volumetric measurement errors and lost axial resolution.

Spherical aberration occurs when light entering the periphery of a spherical lens is focused to a different point on the optical axis than paraxial light rays that enter near the lens's center (Fig. 1a). Lens-induced SA is well understood and is corrected for in the optical components of modern microscopes. However, SA can also be induced by the sample. If converging or diverging light passes through an interface of differing refractive indices (RIs), SA will occur. Two scenarios for imaging through an RI-mismatched interface commonly occur: imaging with an oil immersion objective into a watery live-cell sample and imaging into a high-RI mounting medium or tissue-clearing solution with an air immersion objective. SA created by these types of RI mismatches has three deleterious effects on imaging. First, because all the rays of light originating from a point object do not converge precisely at the image plane, images are dim and blurred. This can be seen in both wide-field (Fig. 1b) and confocal (Fig. 1c) light paths, although the confocal pinhole may reduce axial blur relative to that of wide-field microscopy at the cost of further signal loss. Second, owing to refraction of the more peripheral rays entering the objective—especially at high numerical aperture (NA) values—the nominal focus position (where the focal plane would reside in the absence of refraction) is shifted (Fig. 1b,c). Again, this is seen in both wide-field (Fig. 1b) and confocal (Fig. 1c) microscopes. However, in the confocal microscope, the refraction of both the focusing excitation light and the emitted fluorescence must be considered. The focal shift is related to the NA of the objective and the degree of the RI mismatch. Third, and perhaps most important for 3D imaging, the distance the image plane moves in a sample is not equivalent to the distance traveled by an objective (or stage) during *z*-stack acquisition (Fig. 1d). This non-uniform translation along the *z* axis gives rise to artifactually elongated images (if light travels from a high-RI immersion medium to a lower-RI sample) or compressed images (if imaging from a low-RI immersion medium to a higher-RI sample).

Avoiding spherical aberration–based axial distortion

When preparing samples for a microscopy experiment, the choices of mounting medium and microscope objective are often made independently. Mounting media are primarily chosen on the basis of their antifade properties (ability to prevent photobleaching), whereas objectives are selected on the basis of their theoretical achievable resolution. The resulting RI mismatches have little effect on image quality for thin samples or 2D imaging within a few micrometers of a coverslip. However, 3D fluorescence microscopy images are rapidly degraded by SA if the objective's immersion medium and the sample mounting medium differ in RI or if an incorrect thickness of coverslip is used[1]. Therefore, the choice of immersion medium

[1]Harvard Center for Biological Imaging, Harvard University, Cambridge, MA, USA. [2]Department of Molecular and Cellular Biology, Harvard University, Cambridge, MA, USA. [3]Center for Brain Science, Harvard University, Cambridge, MA, USA. ✉e-mail: drichardson@fas.harvard.edu

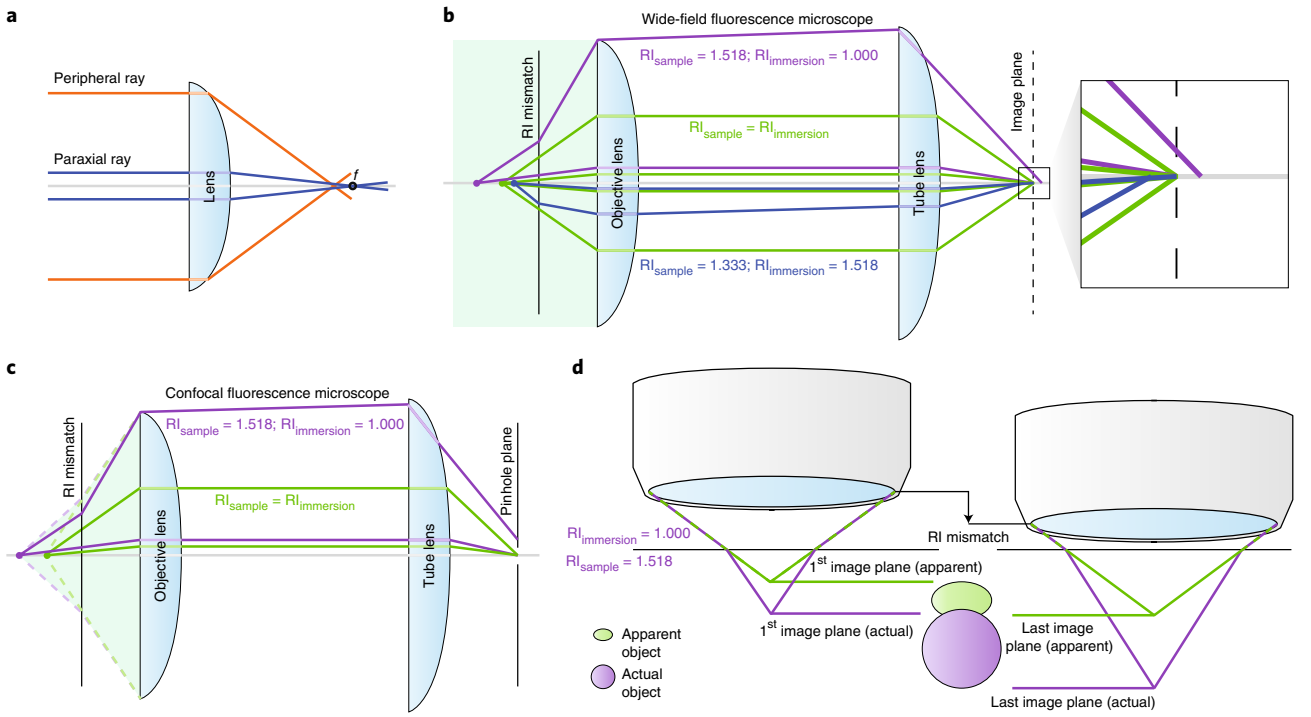

Fig. 1 | Refractive index mismatches induce spherical aberration and axial distortion. a, Lens-based SA occurs when light rays entering near the edge of a lens (peripheral rays, orange) are focused before the focal point (*f*). Light rays entering near the center of the objective (paraxial rays, blue) intersect the optical axis (gray) at the focal point. **b**, Ray trace of light traveling from a point source to the image plane in a wide-field fluorescence microscope. Green shading represents collimated excitation light exiting the objective. Dots (point sources) and lines (ray traces) represent the path light travels when $RI_{sample} > RI_{immersion}$ (purple), $RI_{sample} = RI_{immersion}$ (green), and $RI_{sample} < RI_{immersion}$ (blue). The point source must be located in a different focal plane in each situation to ensure its image is focused near the image plane (dashed line); however, when an RI-mismatched interface exists, SA occurs (see zoomed region, right). **c**, Ray trace of light traveling from a point source to the pinhole plane in a confocal fluorescence microscope. As in **b**, ray tracing diagrams are shown for RI-matched (green) and $RI_{sample} > RI_{immersion}$ (purple) under confocal illumination and detection. In a confocal system, both excitation light (shading within green or purple dashed lines) and emitted fluorescence light rays (green or purple solid lines) undergo refraction if an RI-mismatched interface exists (purple). **d**, An objective is moved axially (black arrow) in a stepwise manner to obtain a 3D image. If there is no change in the RI between the objective and the focal point, no refraction will occur (green lines) and the distance the objective moves (black arrow) is equivalent to the distance moved by the focal plane (green horizontal lines). However, if an RI-mismatched interface exists between the objective and the object to be imaged, refraction occurs, and the focal point is shifted (purple lines). In this scenario, the movement of the objective (black arrow) is not equivalent to the movement of the focal plane (purple horizontal lines). Therefore, when imaging a spherical object ('actual object', purple) that is embedded in a medium with an RI value higher than that of the immersion medium of the objective, a 3D rendering of the object will be compressed in the axial dimension ('apparent object', green) because the acquisition software has assigned the distance of the objective's travel—not the focal plane's travel—to the object's *z* axis.

and objective should be made in unison, with the goal being to match the RI of an objective's immersion medium as closely as possible to the RI of the sample's mounting medium. For example, water immersion or dipping objectives have long been preferred for imaging into living samples because the average RI of a cell (1.360–1.380) is closer to that of water than typical microscope immersion oil[2,3]. Further, many water immersion and dipping objectives have correction collars that can be adjusted to compensate for coverslip thickness, temperature and/or RI mismatch[3,4]. Correction collars therefore extend the useful RI range of a water immersion objective beyond 1.333[3]. Silicone oil immersion objectives (RI = 1.400) offer another alternative for live-cell imaging. The higher RI of silicone oil enables these objectives to be designed with higher NAs, making them particularly suited to super-resolution live-cell imaging[5,6] (see also Table 1). Researchers should take note because sacrificing theoretical resolution by using a lower-NA glycerol immersion objective to image samples in glycerol-based commercial mounting media can produce a higher-quality image compared with using a higher-NA oil immersion objective (see 'Common instances of spherical aberration–based axial distortion in 3D imaging').

A perfect RI match between immersion and mounting medium is not always possible. As an alternative, specialized hardware that can compensate for RI mismatches can be used. A dipping cap can be installed to convert an air objective into a 'pseudo' dipping lens by attaching a cover with a glass window to the sample side of the objective[7]. The glass window is inserted directly into the mounting medium and maintains a constant air gap between the front lens and the mounting medium as the objective moves up and down while imaging the sample, preventing SA-induced axial distortions. Another option is to translate the sample inside a chamber filled with mounting medium while the imaging objective(s) remain(s) stationary outside the chamber[8]. A third option is to place a deformable mirror or spatial light modulator (referred to as

Table 1 | Summary of common refractive indices in microscopy

RIs of common objective immersion media		RIs of common biological samples	
Immersion medium	**RI**	**Sample**	**RI**
Air	1.000	Live tissue	1.360–1.380
Water	1.333	Fixed tissue in glycerol-based mounting medium	1.400–1.470
Silicone oil	1.405	Fixed tissue in high-RI mounting medium	1.520
85% Glycerol	1.456	Aqueous-based cleared tissue	1.380–1.460
Oil	1.518	Solvent-based cleared tissue	1.500–1.560

adaptive optics) to correct the many types of aberrations that can occur across a field of view[9]. Finally, radially symmetric phase masks have been used to equilibrate the SA across all depths of a sample, enabling simplified image restoration by deconvolution after image aquisition[10]. Although these options are useful, they require specialized equipment that may not be an option for every researcher. Therefore, methodologies to correct for axial distortion via post-processing are still required.

Common instances of spherical aberration–based axial distortion in 3D imaging

Throughout this tutorial, we will focus on one historic and two modern RI mismatches in 3D fluorescence microscopy. First, when confocal microscopy was pioneered in the early 1990s, live biological samples (RI = up to 1.380) were primarily imaged with oil immersion objectives (RI = 1.518) because these had the highest NAs and were thought to achieve the highest possible theoretical resolution. As discussed above, the use of oil immersion objectives for live-cell imaging produces an artificial stretching of the data in the axial dimension. Second, modern-day fixed fluorescent samples are primarily mounted in glycerol-based antifade mounting media (RI = 1.400–1.470) and imaged with air (RI = 1.000) or oil (RI = 1.518) immersion objectives. Imaging of this nature will artificially compress (air objective) or stretch (oil objective) the 3D images. Third, imaging of tissue that is millimeters in thickness is now commonplace via advanced confocal and light-sheet microscopy techniques in combination with tissue-clearing approaches (RI = 1.380–1.560) (ref. [11]). In all three of these situations, the RIs of the most common objective immersion media (air, glycerol, oil) rarely match the RI of the sample to be imaged (Table 1). Although oil or glycerol immersion objectives provide a reasonable RI match to many samples, the primary role of these immersion media is to increase the NA of an objective and thus its theoretical resolution. Unfortunately, increasing the NA of an objective results in a decrease in working distance and field of view (unless the diameter of the front lens is also increased). Therefore, most fluid immersion objectives are limited to a working distance of a few hundred micrometers and are incompatible with 3D imaging of thick samples. For these reasons, air objectives are used for imaging thick sectioned and/or cleared tissue because of their long working distances and large fields of view. Air objectives will always induce SA-based axial distortion when used for 3D imaging because the RI of any sample is >1.000 (the RI of air). The appearance of axial distortion from the use of air objectives is therefore quite common in published works. RI mismatches in cleared-tissue imaging are especially hard to avoid (Table 1) and can be found in several published works, including early pioneering studies[12,13]. The artificial compression of 3D images that occurs when imaging into high-RI cleared samples has a severe impact on quantitative measurement of volume and can also affect axial resolution.

Calculating axial distortion correction factors (high to low RI mismatch)

If an RI mismatch cannot be avoided, 3D images must be corrected for axial distortion. SA-based axial distortion of images was first noted during the early development of confocal microscopes. At this time, confocal microscopes primarily used high-NA oil immersion objectives (RI = 1.518) to image live-cell cultures (RI = 1.360–1.380) or fixed-cell cultures (RI = 1.400–1.470) with lower RIs. This RI mismatch resulted in an artificial stretch in the axial dimension during imaging. Using a simple ray optics approach, Carlsson[14] first proposed that this focal shift could be predicted by calculating a correction factor by obtaining the ratio of the RI of a sample's mounting medium to the RI of the imaging objective's immersion medium ($n_{\text{sample}}/n_{\text{immersion}}$). Although Carlsson's calculation provides a good approximation for low-NA objectives, it does not account for the increased axial distortion that is observed with high-NA objectives. Therefore, at high NA, the Carlsson formula underestimates the focal shift. Soon after, Visser et al.[15] developed a formula to calculate axial distortion that considered the NA of the objective (Eq. 1).

$$\Delta_f = \frac{\tan\left(\sin^{-1}\frac{NA}{n_1}\right)}{\tan\left(\sin^{-1}\frac{NA}{n_2}\right)}\Delta_s \quad (1)$$

Here, Δ_f represents the movement of the focal plane within the sample and Δ_s represents the movement of the stage or objective. Unfortunately, Sheppard et al.[16] and Hell et al.[17] later showed that Eq. 1 overestimates the axial distortion at high NA values because it considers only the most peripheral rays emitted from an objective lens and ignores the relatively greater contribution from paraxial rays. In 1993, Hell et al.[17] provided a wave optics solution that is now widely accepted as the most

accurate estimation of axial distortion. Using this method, they were able to predict the decrease in resolution, the decrease in signal intensity and the focal distortion at various imaging depths with high precision. However, wave optics requires complex calculations, and this complexity has probably contributed to the underutilization of this method within the microscopy community. Currently, if microscopists desire to correct an axially distorted image after acquisition, they have the choice of two simple, but inaccurate, equations or one highly complex mathematical formula. Here, we describe two simple modifications to Eq. 1 that can be used to improve its accuracy at high NA and/or large RI mismatches.

Rather than calculating the focal shift of only the most peripheral rays (Visser et al.[15], Eq. 1), we recommend calculating the mean or median depth at which 100 rays equally spaced along the radius of an objective's front lens intersect the optical axis in the sample. We have found that this simple ray optics approach approximates the complex, and difficult to implement, wave optics methods of Hell et al[17] quite well. Therefore, we recommend the use of Eq. 2 (mean) or 3 (median) (see derivation in Supplemental Note 1) for correcting axial distortion when imaging through RI mismatches.

$$\frac{d\prime}{d} = \frac{1}{100} \cdot \sum_{k=1}^{100} \frac{\tan\left(\sin^{-1}\frac{k\mathrm{NA}}{100n_1}\right)}{\tan\left(\sin^{-1}\frac{k\mathrm{NA}}{100n_2}\right)} \quad (2)$$

$$\frac{d\prime}{d} = \frac{\tan\left(\sin^{-1}\frac{0.5\mathrm{NA}}{n_1}\right)}{\tan\left(\sin^{-1}\frac{0.5\mathrm{NA}}{n_2}\right)} \quad (3)$$

In Eqs. 2 and 3, d'/d is a correction factor that relates the actual focal position (d') to the expected focal position (d). k is an integer used to increment through equally spaced rays along the radius of the optical axis. Figure 2 shows that Eqs. 2 and 3 perform better than the ray optics approaches of Carlsson and Visser et al. as compared with the wave optics calculations from Hell et al. In addition, Eqs. 2 and 3 are not biased by high NA values (Fig. 2a) or large differences in RI values (Fig. 2b), as is Eq. 1. Therefore, Eqs. 2 and 3 are simple formulas for estimating the focal shift when imaging from a high (oil immersion) to low (water) RI. We discuss the differences between the mean and median approaches in the 'Mean versus median correction factor' section below.

3D imaging from a high-RI oil immersion medium to a lower-RI live-cell sample is rare today because most researchers know to select water or silicone oil immersion objectives for these types of experiments. However, imaging from a high RI to a low RI in fixed samples is still common. Most commercially available mounting media are glycerol based and have an RI close to 1.450. Clearly, this is poorly matched to the RI of immersion oil (1.518). According to Eqs. 2 and 3, axial correction factors of 0.92 or 0.94, respectively, should be applied to images acquired under these conditions (RI immersion = 1.518; RI sample = 1.45; NA = 1.4). However, in practice the axial distortion of these samples is often minimal because the short working distances of high-NA oil immersion objectives (100–200 μm) limits the maximal axial distortion (stretch) to tens of micrometers.

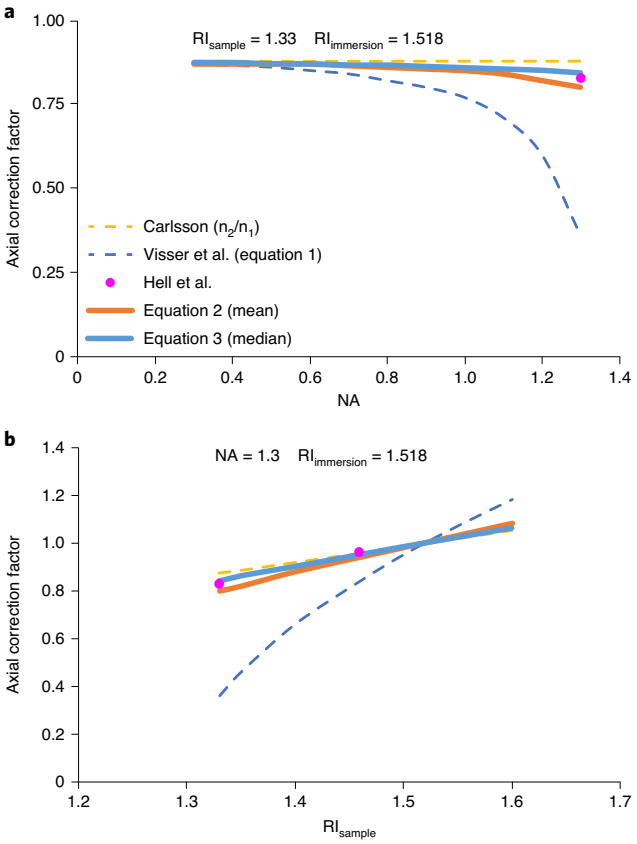

Fig. 2 | Comparison of methods for determining refractive index–mismatch correction factors (high to low refractive index). Correction factors were calculated and plotted using equations and data from Carlsson[14], Visser et al.[15] (Eq. 1), Hell et al.[17] and Eqs. 2 and 3 of the current paper. **a**, The axial correction factor was calculated across NA values of 0.3–1.3 for an oil immersion objective (RI = 1.518) imaging into a solution of RI = 1.33. All methods show close agreement at NA < 0.5. **b**, The axial correction factor was calculated for an NA = 1.3 oil immersion objective imaging into solutions ranging in RI from 1.3 to 1.6. Equations 2 and 3 of the current paper (solid blue and orange lines) show the best agreement with wave optics calculations by Hell et al. (magenta dots).

Calculating axial distortion correction factors (from low to high RI)

Currently, a greater concern is the opposite imaging situation: imaging from a low-RI immersion medium into a high-RI sample. This occurs when air immersion objectives are chosen to facilitate imaging large fields of view (due to lower magnification) or thicker samples (due to longer working distances). It can also occur when immersion objectives are used to image into samples cleared with high-RI tissue-clearing solutions. Therefore, it is important to compare the performance of the various axial distortion correction strategies when imaging from a low-RI immersion medium (such as air) into a high-RI mounting medium or tissue-clearing solution. To our knowledge, a wave optics approach has not been applied to this low

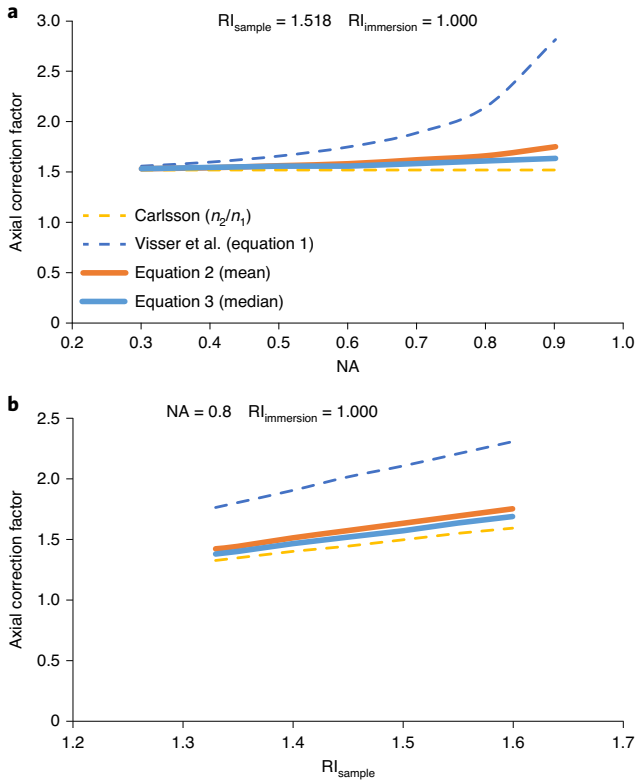

Fig. 3 | Comparison of methods for determining refractive index mismatch correction factors (low to high refractive index). Correction factors were calculated and plotted using equations and data from Carlsson[14], Visser et al.[15] (Eq. 1), and Eqs. 2 and 3 of the current paper. **a**, The axial correction factor was calculated across NA values of 0.3–0.9 for an air immersion objective (RI = 1.000) imaging into a solution of RI = 1.518. **b**, The axial correction factor was similarly calculated for an NA = 0.8 air immersion objective (RI = 1.000) imaging into solutions ranging in RI from 1.33 to 1.60.

RI to high RI imaging scenario. However, ray optics can be easily extended to this context. Figure 3 displays correction factors for imaging into high-RI samples with air immersion objectives calculated with the same ray optics approaches used in Fig. 2. Again, the Carlson and Visser equations appear to underestimate or overestimate, respectively, the correction factor at high NA values.

Experimental demonstration of correcting axial distortions

Validation using fluorescent beads

To confirm the validity of Eqs. 2 and 3 when imaging from low to high RI, a simple experiment can be performed. Fluorescent beads are fixed to a microscope slide and overlaid with solutions of differing RI (see Supplementary Methods). A coverslip is then placed above these solutions on a spacer (Fig. 4a). If a 3D field of view is imaged at the interface of these solutions and the neighboring empty space, the focal shift due to SA can be calculated. Figure 4b displays such an experiment, in which 2-μm fluorescent beads were placed 200 μm below a coverslip. Droplets of immersion media with RI = 1.333 and RI = 1.518 were placed over the beads. When images were taken at the interface of these solutions with a 0.45-NA air immersion objective, the beads in high-RI medium (1.333 or 1.518) appeared elevated above the glass slide relative to those residing in air (Fig. 4b–d). In this example (RI immersion = 1.000; RI sample = 1.000, 1.333 or 1.518; and NA = 0.45), Eqs. 2 and 3 calculate nearly identical correction factors for the following conditions: 1.00 (beads in air), 1.35 (beads in RI = 1.333), and 1.54 (Eq. 3) or 1.55 (Eq. 2) (beads in RI = 1.518). If Eqs. 2 and 3 are accurate, multiplying the z spacing of the images by the correction factor should restore the beads to their correct axial positions. Figure 4c (right panels) and 4d show exactly this (using Eq. 2). Therefore, Eqs. 2 and 3 can be used to correct 3D volumetric data that is distorted by imaging from a low-RI immersion medium into a high-RI sample.

Correcting axial distortion in 3D volumes

Figure 1d depicts how SA causes the image plane to move through a sample at a different rate than the objective (or stage) travels during 3D image acquisition. This mismatched travel speed results in an SA-induced z-axis elongation or compression that must be corrected before performing quantitative volumetric analysis. Figure 5a illustrates one of the common experimental conditions discussed above: imaging a sample in a glycerol-based commercial mounting medium (RI = 1.460). If a glycerol objective is chosen, the immersion medium is well matched to the RI of the mounting medium and no axial distortion correction is required. Here, a measurement along the z axis represents the true thickness of the tissue section (Fig. 5a). When the exact same region is imaged with an air immersion objective of equivalent NA, the resulting image is axially compressed to approximately 60% of its actual thickness (Fig. 5a). To correct for this compression, a correction factor should be calculated using Eq. 2 or 3 and the values RI immersion = 1.000, RI sample = 1.460, and NA = 0.8. Next, the z step of the acquired image is multiplied by the correction factor (1.59, via Eq. 2) to stretch the image to its actual thickness (Fig. 5a, compare air immersion original (Org) with z-corrected (Zcor)). Similarly, when imaging a cleared organoid (clearing solution RI = 1.560, see Supplementary Methods) with a 0.45-NA air immersion objective, the raw data are artificially compressed in the axial dimension. Volumetric analysis of the original and corrected images suggests the volume of the organoid is underestimated by more than 1.5× if uncorrected (Fig. 5b). A correction factor of 1.59 (calculated using Eq. 2) adjusts the axial dimension of the image, and a more accurate estimation of the spheroid's volume is obtained. Therefore, before performing volumetric measurements on 3D images acquired through an RI-mismatched interface, it is essential that the axial distortion be first corrected following the methods outlined below.

Experimental demonstration of determining axial sampling rates

Effect of spherical aberration on axial sampling

SA-induced distortion can also affect the achievable axial resolution of a microscope. Because the movement of the focal

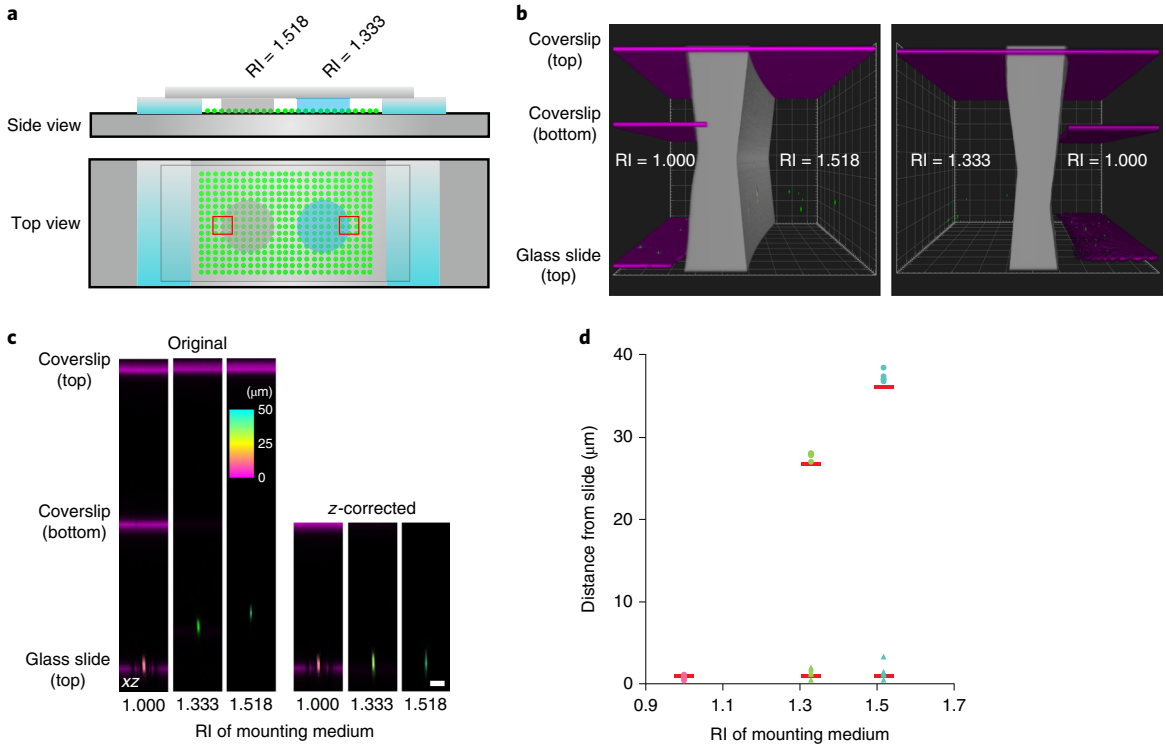

Fig. 4 | Refractive index mismatches induce a focal shift. a, Diagram of the fluorescent bead preparation for measuring focal shift in media of various RI values. Fluorescent beads (green circles) were adhered to a microscope slide between double-sided tape spacers (Supplementary Methods). Drops of RI = 1.333 (blue) and RI = 1.518 (gray) liquids were placed over the beads. A no. 1.5 coverslip was placed on the liquid drops and spacers. Red boxes indicate areas of air–liquid interfaces, where multiple beads residing in both RIs could be imaged in a single field of view. **b**, 3D rendering of volumes captured at the air–liquid interface, as indicated in **a**, using 200-μm spacers. The left panel images through a liquid with RI = 1.518, and the right panel images through RI = 1.333. Beads (2 μm; green) were visualized by fluorescence microscopy; the coverslip and glass slide surfaces were visualized by reflected light imaging (magenta), and the edge of the droplet was detected via transmitted light (intensity is inverted and pseudo-colored gray; see Supplementary Methods). Beads appear elevated when overlaid with solution. White boxes are 40 μm^2. **c**, The experiment in **b** was repeated with a 100-μm spacer. Orthogonal (*xz*) color-coded depth projections of individual fluorescent beads are presented. The color of the bead indicates its distance from the glass slide according to the color scale. Reflections from the coverslip and microscope slide are shown in magenta. *z*-corrected images of the 1.333- and 1.518-RI embedded beads are also shown in the right-hand panels. Scale bar, 10 μm. **d**, Distance from the glass slide (apparent focal shift) was calculated and plotted for five beads outside the liquid drops (RI = 1.000, pink dots), five beads in the RI = 1.333 medium (green dots), and five beads in the RI = 1.518 medium (cyan dots). The distances between the beads in RI = 1.333 and RI = 1.518 and the slide were remeasured after applying a *z* correction as in **c** (green and cyan triangles, respectively). Red bars indicate the expected bead positions predicted by Eq. 2.

plane within a sample is accelerated or decelerated relative to the physical movement of the objective, the optimal *z* step (axial sampling rate) must be adjusted accordingly. It is well understood that to maximize the resolution of a microscope in any dimension, the sampling rate (number of pixels) must be at least twice the theoretical resolution limit of the imaging system (referred to as Nyquist sampling). Several equations (for an example, see Supplementary Note 2) can be used to determine the correct *z* step. Commercial microscope software uses these equations to recommend an 'optimal' axial sampling rate. Unfortunately, these equations will recommend too small (if imaging from high to low RI) or too large (if imaging from low to high RI) of a *z* step when imaging through an RI-mismatched interface. Therefore, when imaging into a lower-RI sample (relative to the immersion medium of the objective), the *z* planes will be too close together, and excessive photobleaching or phototoxicity may be induced in the sample. Conversely, when imaging into a higher RI sample, the *z* step will be too large, and the achievable resolution of the microscope will be reduced. Figure 5c demonstrates that imaging at the suggested *z* step fails to resolve all labeled axons in an axial (*xz*) maximum intensity projection of a thick tissue volume. All images were corrected after imaging for axial distortion, demonstrating that the sampling rate must be determined before, not after, imaging is performed.

Correct axial sampling improves segmentation

The initial step of most image analysis routines is to segment objects of interest. Failure to adjust the axial sampling rate (*z* step) according to any RI-mismatches that exist between the sample and the objective's immersion medium will impact a researcher's ability to properly segment individual objects. Figure 6a displays an automated segmentation of the image in Fig. 5c. More objects are segmented (12 versus 7) when the correct axial sampling rate is calculated before imaging and the *z* spacing is corrected after acquisition. The increase in the

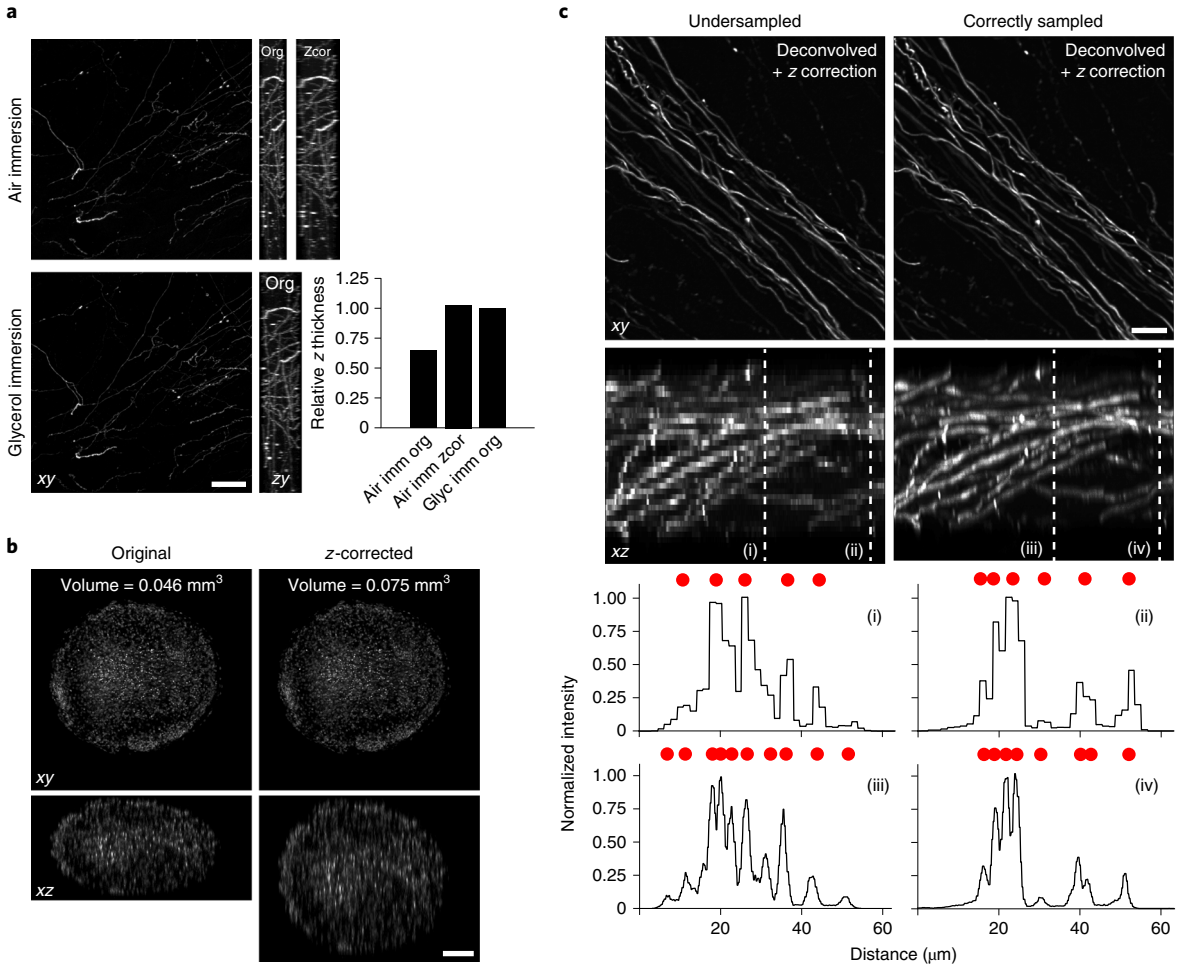

Fig. 5 | Refractive index mismatches induce spherical aberration and axial distortion. a, A 50-μm-thick region of mouse brain tissue expressing the tdTomato fluorescent protein in a subset of neurons was imaged with a 20× 0.8-NA air or a 25× 0.8-NA glycerol immersion objective (Supplementary Methods). Gamma-adjusted (0.5) maximum intensity projections are displayed for the lateral (*xy*) and axial (*zy*) planes. The *zy* plane is shown before (Org) and after (Zcor) *z*-axis compression correction for the air objective. The relative thickness (*z* dimension), normalized to the glycerol immersion projection (Glyc Imm Org), is displayed for the air immersion objective's original (Air Imm Org) and *z*-corrected (Air Imm Zcor) projections. Scale bar, 50 μm. **b**, Lateral (*xy*) and axial (*xz*) slices through an organoid labeled with the SiR-DNA nuclear dye are presented. Organoids were cleared (Supplementary Methods) and imaged in dibenzyl ether (RI = 1.560) with a 10× 0.45-NA objective. Volumetric measurements were calculated for 3D-rendered uncorrected and *z*-corrected datasets. Scale bar, 100 μm. **c**, Lateral (*xy*) and axial (*xz*) maximum intensity projections were calculated for confocal image stacks acquired through the same mouse brain section as in **a**. The volume was imaged twice: (1) using the manufacturer's recommended *z* step (undersampled) and (2) at an adjusted *z* step that accounts for SA-induced focal shift (see Supplementary Note 2). To quantitate the number of neuronal processes resolved under different sampling conditions, pixel intensity profiles were determined along the indicated dotted lines and plotted; Roman numerals in the images correspond to those in the plots. Red dots represent individually resolved axons. Scale bar, 10 μm.

number of segmented objects results for two reasons. First, in an undersampled dataset, thin objects that lie parallel to the lateral plane may appear on only a single (or very few) slice(s). Therefore, the object's 3D volume is small and falls below the volume threshold value that is set to exclude small, artifactual objects. If an object's volume is below the set threshold, it is deemed too small to be relevant and is excluded. These objects cannot be recovered by lowering the threshold because the image becomes overwhelmed with small punctate structures that often represent debris or staining artifacts. In Fig. 6a, the threshold was set to 10,000 pixels. Four thin objects that lie in the lateral plane can be segmented only in the properly sampled dataset (Fig. 6a, right panel, white arrowheads). Second, objects lying directly above one another can falsely appear connected if the axial sampling rate is insufficient to resolve both structures. Figure 6b displays two axons that could not be segmented in the undersampled dataset but are clearly two separate objects when the sample is reimaged at the correct axial sampling rate. Therefore, it is critical to calculate an adjusted axial sampling rate (*z* step) before imaging to ensure optimal axial resolution as described in the methods outlined below. It is essential to understand that axial resolution cannot be increased or recovered through post-processing if the original image is under sampled.

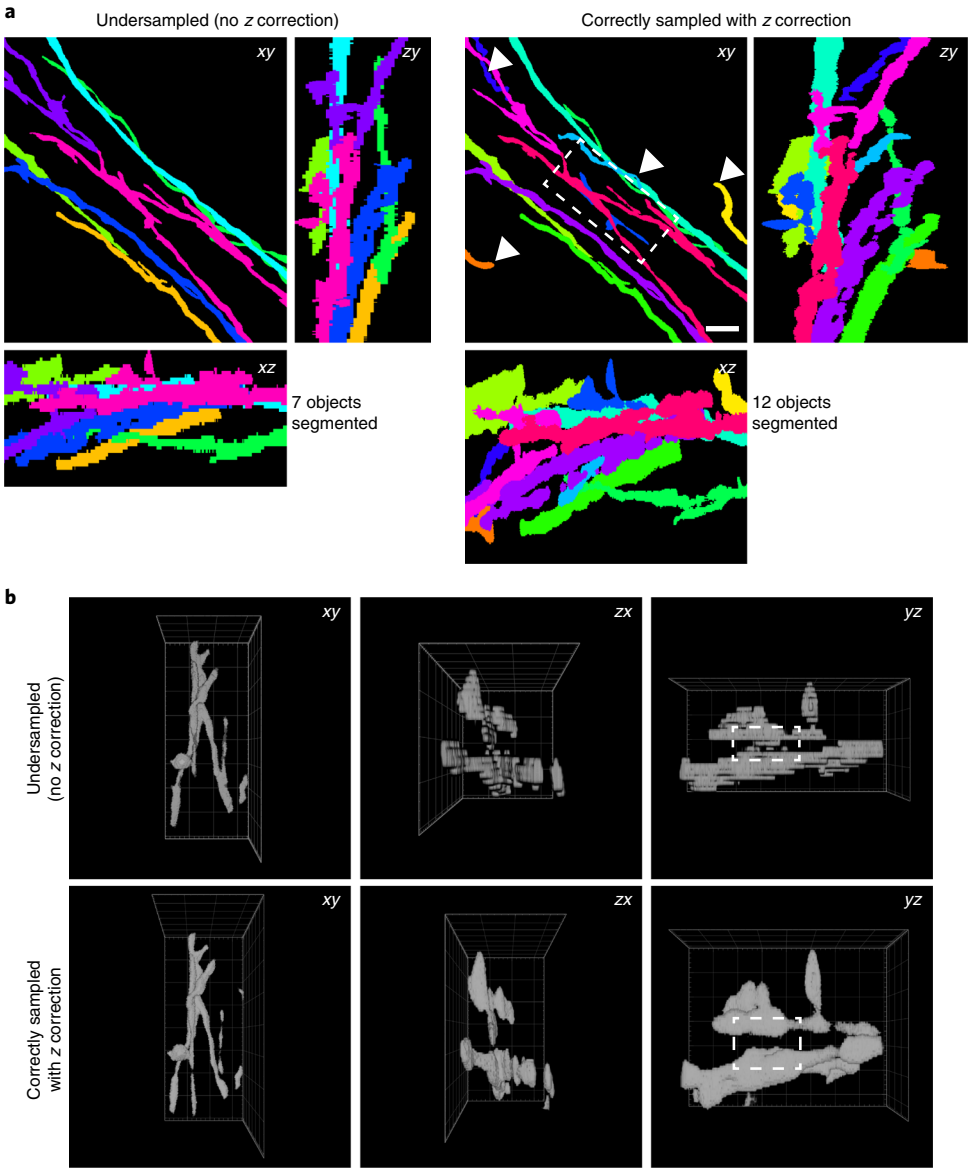

Fig. 6 | Correcting axial sampling improves segmentation. a, An N-class thresholding based on k-means classification (hierarchical k-means, Icy (http://icy.bioimageanalysis.org/download/)) automated segmentation routine was applied to the data in Fig. 5c. Each color represents an individually segmented object. Maximum intensity projections of the volume are presented along the *xy*, *xz*, and *zy* planes. White arrowheads indicate thin objects that are excluded in the undersampled dataset because of their *z* compression. Scale bar, 10 μm. **b**, 3D renderings of the white boxed region in **a** (right-hand *xy* image). Volume renderings along the *xy*, *zx*, and *yz* axes are shown. White dashed boxes in the *yz* images highlight an area that is poorly segmented in the undersampled data. White grids in background measure 10 × 10 μm.

An ImageJ/Fiji-based macro for axial distortion correction and optimal *z*-step determination

Equations 2 and 3 allow less complex calculations than wave optics methods but are still not simple enough for rapid manual calculation. Therefore, we have developed an ImageJ/Fiji-based[18,19] macro that allows researchers to (i) ensure the highest achievable axial resolution and prevent excess phototoxicity by calculating the optimal *z* step for their experiment before imaging and (ii) correct any axial distortions (compression or stretch) after imaging (see Box 1 for a step-by-step procedure for installation and application of the macro). The macro is run before imaging to calculate an optimal axial sampling rate (use the 'Provide recomended Z-step only' option as indicated in Box 1, step 8A(iv)). After imaging is complete, the macro is rerun to adjust the *z* spacing of the acquired dataset and correct SA-induced axial distortion using Eqs. 2 and/or 3 (Box 1, step 8A(viii–xiv)). If sufficient metadata exist, the macro will warn users if their acquisition *z* step was too large during imaging and thus limited the achievable axial resolution.

Mean versus median correction factor

Equations 2 and 3 present two ray optics–based approaches for calculating a correction factor for SA-induced axial distortion.

Box 1 | Installation and application of the focal shift correction macro ● Timing Installation: 15 min; calculate sampling rate: 2 min; correcting axial distortion: minutes to hours depending on number and size of files

This box provides a step-by-step procedure for the installation (Steps 1–7) and use (Step 8) of the macro. The source code can be copied directly from the Supplementary Software. Correct use of the macro before image acquisition (Step 8A(i–v)) will ensure that the full resolving power of the microscope is utilized. Following acquisition, Step 8A(vii–xiv) describes how to correct RI mismatch-induced axial distortion before 3D visualization and analysis. Alternatively, the post-acquisition processing steps can be avoided if a microscope's control software allows the input of RI-mismatch correction factors (Step 8B).

Macro installation procedure

1 Install or update to the current version of ImageJ[19] (https://imagej.nih.gov/ij/download.html) or Fiji[18] (https://fiji.sc/). If using ImageJ, you must also install a current version of the Bioformats plugin (https://docs.openmicroscopy.org/bio-formats/5.8.2/users/imagej/installing.html).
2 Open ImageJ/Fiji.
3 Open a new macro editor window ('Plugins' > 'New' > 'Macro').
4 Copy the source code from the Supplementary Software and paste it into the macro editor window.
5 On the 'Language' dropdown menu, select 'IJ1 Macro'.
6 Click 'File' > 'Save as' and save the macro to the ImageJ 'plugins' folder. The file name must contain an underscore ('_').
7 Restart ImageJ/Fiji and locate the macro at the bottom of the 'Plugins' dropdown menu.

Procedure for using the macro

8 To use the macro to calculate an optimal axial sampling rate (before image acquisition) and correct axially distorted images after acquisition, follow option A. To use the macro in conjunction with microscope control software that allows user-input RI mismatch correction factors, follow option B.

(A) **Using the macro to calculate an optimal axial sampling rate and correct axially distorted images**

(i) Ensure that the macro is saved in the ImageJ/Fiji 'plugins' folder (see step 6 above).
(ii) Run the macro by selecting it from the 'Plugins' menu.
(iii) Fill in the requested information as shown in the example screenshot below:

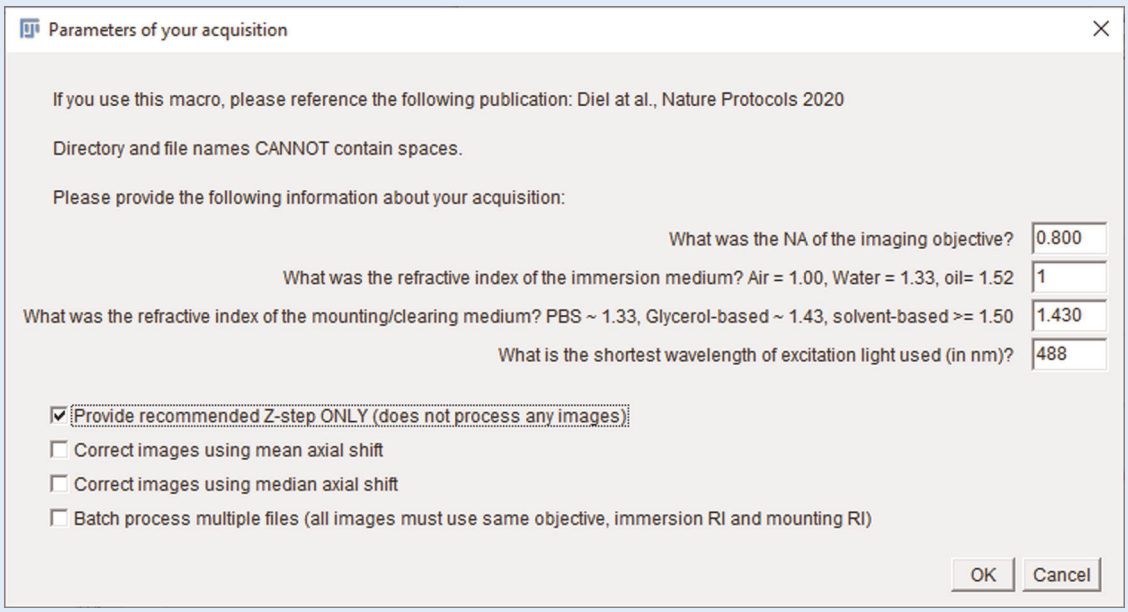

(iv) Check 'Provide recommended Z-step ONLY' to output the recommended *z* step without processing any data.
(v) Click 'OK'. The recommended *z* step will be printed in the ImageJ/Fiji 'Log' window.
(vi) Proceed to the microscope to image the sample.
(vii) Enter the macro's recommended *z* step into the corresponding location of the microscope control software.
(viii) Once imaging is completed, place all Bioformats-compatible image files (such as ome.tif, .czi, .lif, .nd2, .oif files) to be processed into a single folder (directories, subdirectories and files names must not contain spaces).
(ix) Create an empty 'output' folder.
(x) Run the macro by selecting it from the 'Plugins' menu in ImageJ/Fiji.
(xi) Fill in the requested information as shown in the example screenshot above (step 8A(iii)).
(xii) Check 'Correct images using mean axial shift' to use Eq. 2 (mean) and/or 'Correct images using median axial shift' to use Eq. 3 (median) when calculating the *z*-correction factor.
(xiii) Check 'Batch process multiple files' if more than one image is to be processed (all images must have been acquired using the same conditions: NA, immersion RI, mounting RI) and click 'OK'.
(xiv) Locate the input and output folders when requested. The corrected images will be saved to the output folder as .tif stacks and can be opened directly.

Box 1 | (continued)

(B) **Using the macro together with microscope acquisition software with an RI mismatch correction function**

(i) Ensure that the macro is saved in the ImageJ/Fiji 'plugins' folder (see step 6 above).
(ii) Run the macro by selecting it from the 'Plugins' menu.
(iii) Fill in the requested information as shown in the example screenshot above.
(iv) Check 'Provide recommended Z-step ONLY'.
(v) Click 'OK'. Along with the recommended *z* step, an axial distortion correction factor will be printed in the ImageJ/Fiji 'Log' window.
(vi) Proceed to the microscope to image the sample.
(vii) Enter the macro's recommended *z* step in the corresponding location of the microscope control software.
(viii) Enter the macro's recommended axial correction factor in the corresponding location of the microscope control software (screenshot below displays location for Carl Zeiss' ZEN Black or Blue software).

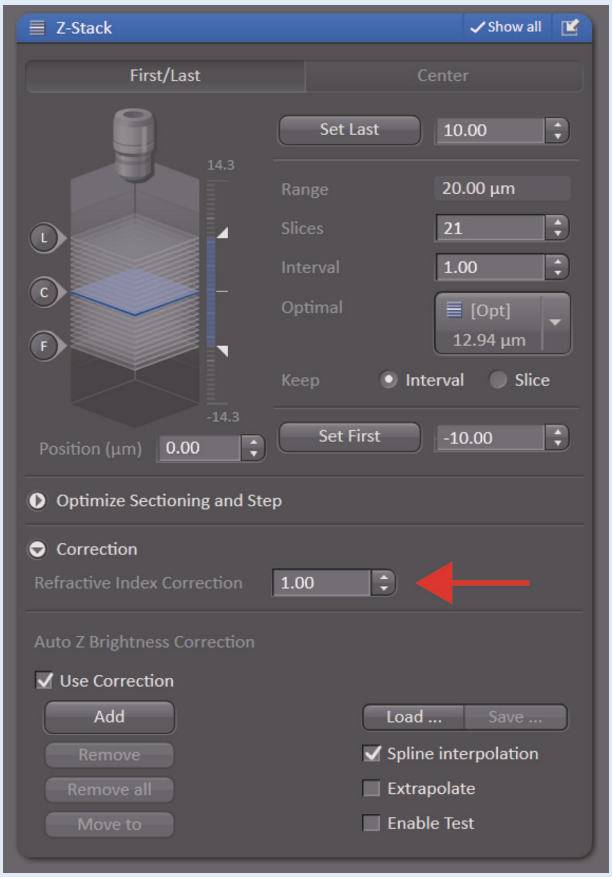

(ix) No further processing is required after image acquisition.

Equation 2 calculates the mean intersection point of 100 rays with the optical axis, whereas Eq. 3 calculates the median intersection point. For objectives with low NA (< ~0.5) imaging through minimal RI mismatches (< ~0.15), the two methods calculate nearly identical correction factors (Fig. 2). At higher NA (>0.5) and larger RI mismatches (>0.15), Eqs. 2 and 3 differ slightly but agree well with the wave optics calculations of Hell et al. (Fig. 2). Equation 2 calculates a higher degree of correction at high NA and large RI differences, whereas Eq. 3 (median) determines less correction is required relative to wave optics. Of the ray optics approaches investigated here, Eqs. 2 and 3 show the closest agreement to wave optics calculations across various NAs and RIs when imaging from a high-RI medium into a lower-RI sample (Fig. 2). The differences in correction factors calculated by Eqs. 2 and 3 and wave optics formulas are minimal. For example, the calculated focal shift for a 1.3-NA oil immersion objective imaging into a RI = 1.333 water solution are all within 20 nm of one another, well below the resolving power of the microscope. Although we do not have wave optics data for the inverse situation (imaging from a low-RI immersion medium into a higher-RI sample), Eqs. 2 and 3 are still in good agreement with one another (Fig. 3). Both equations show a response to increasing NA (unlike Carlsson), but neither is as heavily influenced by NA as Visser et al. (Fig. 3a). Therefore, Eqs. 1 and 2 provide accurate correction factors for imaging through high to low or low to high RI mismatches.

Limitations of the macro

The macro is not able to correct the lateral or axial blur that is introduced by SA or improve lateral or axial resolution after acquisition. SA-induced blur increases with objective NA and imaging depth. Increases in computing power now allow deconvolution to be applied to large 3D datasets, and deconvolution has been used to correct for the blur and axial shift induced by SA. SA correction via deconvolution requires a model of the blur introduced by SA and other factors such as diffraction within the entire optical path (microscope and sample), called the point spread function (PSF). Theoretical PSFs can be calculated, but they do not always consider SA and are commonly isometric in the axial dimension. Therefore, care must be taken when using theoretical PSFs to ensure that a model of SA blur is included and that axial shifts are corrected. Both open-source and commercial software are available for performing this level of deconvolution[20,21]. In addition, experimentally determined PSFs can be measured and used for deconvolution. Experimental PSFs can be obtained by imaging beads submerged in the sample mounting medium at various depths under a coverslip (Fig. 4a). For relatively thin samples, beads placed at a depth of half the sample's thickness may suffice. For thick samples, PSFs measured at multiple distances may be necessary[22–24].

Reporting Summary

Further information on research design is available in the Nature Research Reporting Summary linked to this article.

Data availability

All original (raw) data are available from the authors upon reasonable request.

Code availability

All necessary code and instructions for running the axial correction macro are provided in the Supplementary Software and Box 1.

References

1. Gibson, S. F. & Lanni, F. Experimental test of an analytical model of aberration in an oil-immersion objective lens used in three-dimensional light microscopy. *J. Opt. Soc. Am. A* **9**, 154–166 (1992).
2. Zhang, Q. et al. Quantitative refractive index distribution of single cell by combining phase-shifting interferometry and AFM imaging. *Sci. Rep.* **7**, 2532 (2017).
3. Keller, H. E. Objectives for confocal microscopy. in *Handbook of Biological Confocal Microscopy* (ed Pawley, J. B.) (Springer, 1995).
4. Jonkman, J., Brown, C. M., Wright, G. D., Anderson, K. I. & North, A. J. Tutorial: guidance for quantitative confocal microscopy. *Nat. Protoc.* **15**, 1585–1611 (2020).
5. Heine, J. et al. Three dimensional live-cell STED microscopy at increased depth using a water immersion objective. *Rev. Sci. Instrum.* **89**, 053701 (2018).
6. Schmidt, N. C., Kahms, M., Huve, J. & Klingauf, J. Intrinsic refractive index matched 3D dSTORM with two objectives: comparison of detection techniques. *Sci. Rep.* **8**, 13343 (2018).
7. Dodt, H. U. et al. Ultramicroscopy: development and outlook. *Neurophotonics* **2**, 041407 (2015).
8. Engelbrecht, C. J. & Stelzer, E. H. Resolution enhancement in a light-sheet-based microscope (SPIM). *Opt. Lett.* **31**, 1477–1479 (2006).
9. Ji, N. Adaptive optical fluorescence microscopy. *Nat. Methods* **14**, 374–380 (2017).
10. Patwary, N., King, S. V., Saavedra, G. & Preza, C. Reducing effects of aberration in 3D fluorescence imaging using wavefront coding with a radially symmetric phase mask. *Opt. Express* **24**, 12905–12921 (2016).
11. Richardson, D. S. & Lichtman, J. W. Clarifying tissue clearing. *Cell* **162**, 246–257 (2015).
12. Chung, K. et al. Structural and molecular interrogation of intact biological systems. *Nature* **497**, 332–337 (2013).
13. Renier, N. et al. iDISCO: a simple, rapid method to immunolabel large tissue samples for volume imaging. *Cell* **159**, 896–910 (2014).
14. Carlsson, K. The influence of specimen refractive-index, detector signal integration, and nonuniform scan speed on the imaging properties in confocal microscopy. *J Microsc.-Oxford* **163**, 167–178 (1991).
15. Visser, T. D., Oud, J. L. & Brakenhoff, G. J. Refractive-index and axial distance measurements in 3-D microscopy. *Optik* **90**, 17–19 (1992).
16. Sheppard, C. J., Gu, M., Brain, K. & Zhou, H. Influence of spherical aberration on axial imaging of confocal reflection microscopy. *Appl. Opt.* **33**, 616–624 (1994).
17. Hell, S., Reiner, G., Cremer, C. & Stelzer, E. H. K. Aberrations in confocal fluorescence microscopy induced by mismatches in refractive-index. *J. Microsc.* **169**, 391–405 (1993).
18. Schindelin, J. et al. Fiji: an open-source platform for biological-image analysis. *Nat. Methods* **9**, 676–682 (2012).
19. Schneider, C. A., Rasband, W. S. & Eliceiri, K. W. NIH Image to ImageJ: 25 years of image analysis. *Nat. Methods* **9**, 671–675 (2012).
20. Ghosh, S. & Preza, C. Fluorescence microscopy point spread function model accounting for aberrations due to refractive index variability within a specimen. *J. Biomed. Opt.* **20**, 75003 (2015).
21. Model, M. A., Fang, J., Yuvaraj, P., Chen, Y. & Zhang Newby, B. M. 3D deconvolution of spherically aberrated images using commercial software. *J. Microsc.* **241**, 94–100 (2011).
22. Kim, B. & Naemura, T. Blind depth-variant deconvolution of 3D data in wide-field fluorescence microscopy. *Sci. Rep.* **5**, 9894 (2015).
23. Preza, C. & Conchello, J. A. Depth-variant maximum-likelihood restoration for three-dimensional fluorescence microscopy. *J. Opt. Soc. Am. A* **21**, 1593–1601 (2004).
24. Ghosh, S. & Preza, C. Three-dimensional block-based restoration integrated with wide-field fluorescence microscopy for the investigation of thick specimens with spatially variant refractive index. *J. Biomed. Opt.* **21**, 46010 (2016).

Acknowledgements

We thank S. Piccinotti and L. Rubin for providing organoid samples. We thank the Harvard Center for Biological Imaging for infrastructure and support. J.W.L. was supported by the following funding sources: National Institutes of Health grants P50 MH094271, U24 NS109102, and U19 NS104653 and Department of Defense MURI award GG008784.

Author contributions

The idea for calculating axial distortion correction factors as described in this tutorial was conceived by D.S.R. and J.W.L. E.E.D. and D.S.R. carried out experiments and analyzed data. D.S.R., J.W.L. and E.E.D. wrote the manuscript. All authors contributed to editing the final manuscript.

Competing interests

The authors declare no competing interests.

Additional information

Supplementary information is available for this paper at https://doi.org/10.1038/s41596-020-0360-2.

Correspondence and requests for materials should be addressed to D.S.R.

Peer review information *Nature Protocols* thanks Chrysanthe Preza and the other, anonymous, reviewer(s) for their contribution to the peer review of this work.

Received: 15 October 2019; Accepted: 18 May 2020;
Published online: 31 July 2020

Related links

References that contributed to the development of this protocol

Visser, T. D. et al. *Optik* **90**, 17–19 (1992): https://www.researchgate.net/publication/285251956_Refractive_index_and_axial_distance_measurements_in_3-D_microscopy

Hell, S., Reiner, G., Cremer, C. & Stelzer, E. H. K. *J. Microsc.* **169**, 391–405, (1993): https://onlinelibrary.wiley.com/doi/abs/10.1111/j.1365-2818.1993.tb03315.x

nature research

Corresponding author(s): Douglas S Richardson

Last updated by author(s): Apr 8, 2020

Reporting Summary

Nature Research wishes to improve the reproducibility of the work that we publish. This form provides structure for consistency and transparency in reporting. For further information on Nature Research policies, see Authors & Referees and the Editorial Policy Checklist.

Statistics

For all statistical analyses, confirm that the following items are present in the figure legend, table legend, main text, or Methods section.

n/a	Confirmed
☐	☒ The exact sample size (*n*) for each experimental group/condition, given as a discrete number and unit of measurement
☐	☒ A statement on whether measurements were taken from distinct samples or whether the same sample was measured repeatedly
☒	☐ The statistical test(s) used AND whether they are one- or two-sided *Only common tests should be described solely by name; describe more complex techniques in the Methods section.*
☒	☐ A description of all covariates tested
☒	☐ A description of any assumptions or corrections, such as tests of normality and adjustment for multiple comparisons
☒	☐ A full description of the statistical parameters including central tendency (e.g. means) or other basic estimates (e.g. regression coefficient) AND variation (e.g. standard deviation) or associated estimates of uncertainty (e.g. confidence intervals)
☒	☐ For null hypothesis testing, the test statistic (e.g. *F*, *t*, *r*) with confidence intervals, effect sizes, degrees of freedom and *P* value noted *Give P values as exact values whenever suitable.*
☒	☐ For Bayesian analysis, information on the choice of priors and Markov chain Monte Carlo settings
☒	☐ For hierarchical and complex designs, identification of the appropriate level for tests and full reporting of outcomes
☒	☐ Estimates of effect sizes (e.g. Cohen's *d*, Pearson's *r*), indicating how they were calculated

Our web collection on statistics for biologists contains articles on many of the points above.

Software and code

Policy information about availability of computer code

Data collection	ZEN Black version 2.6 (Carl Zeiss Microscopy) microscope control software was used for image acquisition.
Data analysis	Vision 4D version 3.1 (arivis AG), Fiji version 1.52p and Icy version 2.0.3.0 were used for image analysis

For manuscripts utilizing custom algorithms or software that are central to the research but not yet described in published literature, software must be made available to editors/reviewers. We strongly encourage code deposition in a community repository (e.g. GitHub). See the Nature Research guidelines for submitting code & software for further information.

Data

Policy information about availability of data

All manuscripts must include a data availability statement. This statement should provide the following information, where applicable:

- Accession codes, unique identifiers, or web links for publicly available datasets
- A list of figures that have associated raw data
- A description of any restrictions on data availability

All original (raw) data is available from the authors upon reasonable request.

Field-specific reporting

Please select the one below that is the best fit for your research. If you are not sure, read the appropriate sections before making your selection.

☒ Life sciences ☐ Behavioural & social sciences ☐ Ecological, evolutionary & environmental sciences

Life sciences study design

All studies must disclose on these points even when the disclosure is negative.

Sample size	3-5 data points were measured for each experimental condition. All data points showed little variability and closely agreed with calculated theoretical values. Therefore, these sample sizes were deemed sufficient.
Data exclusions	No data was excluded.
Replication	All replications were successful and agreed closely to theoretical calculations. All individual data points are reported in the figures.
Randomization	No statistical analysis was done to compare groups. All measurements were compared to theoretical calculations.
Blinding	Blinding was not relevant as no statistical analysis was done to compare groups.

Reporting for specific materials, systems and methods

We require information from authors about some types of materials, experimental systems and methods used in many studies. Here, indicate whether each material, system or method listed is relevant to your study. If you are not sure if a list item applies to your research, read the appropriate section before selecting a response.

Materials & experimental systems

n/a	Involved in the study
☒	☐ Antibodies
☒	☐ Eukaryotic cell lines
☒	☐ Palaeontology
☐	☒ Animals and other organisms
☒	☐ Human research participants
☒	☐ Clinical data

Methods

n/a	Involved in the study
☒	☐ ChIP-seq
☒	☐ Flow cytometry
☒	☐ MRI-based neuroimaging

Animals and other organisms

Policy information about studies involving animals; ARRIVE guidelines recommended for reporting animal research

Laboratory animals	Adult C57BL/6J male mice were used
Wild animals	Study did not involve wild animals
Field-collected samples	Study did not include field-collected samples
Ethics oversight	All experiments were conducted in accordance with procedures approved by the Institutional Animal Care and Use Committees of Harvard University.

Note that full information on the approval of the study protocol must also be provided in the manuscript.